Astronomy & Astrophysics

Accretion discs onto supermassive compact objects: A portal to dark matter physics in active galaxies

C. Millauro[1], C. R. Argüelles[2,3] , F. L. Vieyro[4,5] , V. Crespi[5] , and M. F. Mestre[3,5]

[1] Departamento de Física, Facultad de Ciencias Exactas y Naturales, Universidad de Buenos Aires, Pabellón I, Ciudad Universitaria, 1428 Buenos Aires, Argentina
[2] ICRANet, Piazza della Repubbli ca 10, 65122 Pescara, Italy
[3] Instituto de Astrofísica de La Plata, UNLP & CONICET, Paseo del Bosque, B1900FWA La Plata, Argentina
e-mail: `carguelles@fcaglp.unlp.edu.ar`
[4] Instituto Argentino de Radioastronomía (IAR, CONICET/CIC/UNLP), C.C.5, (1894) Villa Elisa, Buenos Aires, Argentina
[5] Fac. de Ciencias Astron. y Geofísicas, Universidad Nacional de La Plata, Paseo del Bosque, B1900FWA La Plata, Argentina

ABSTRACT

Context. The study of the physics of the accretion discs that develop around supermassive black hole (BH) candidates provides essential theoretical tools to test their nature.
Aims. Here, we study the accretion flow and associated emission using generalised α-discs accreting onto horizonless dark compact objects in order to make comparisons with the traditional BH scenario. The BH alternative proposed here consists in a dense and highly degenerate core made of fermionic dark matter (DM) and surrounded by a more diluted DM halo. This dense core–diluted halo DM configuration is a solution of Einstein's equation of general relativity (GR) in spherical symmetry, which naturally arises once the quantum nature of the DM fermions is duly accounted for.
Methods. The methodology followed in this work consists in first generalising the theory of α-discs to work in the presence of regular and horizonless compact objects, and then applying it to the case of core–halo DM profiles typical of active-like galaxies.
Results. The fact that the compactness of the dense and transparent DM core scales with particle mass allows the following key findings of this work: (i) There is always a given core compacity – corresponding particle mass – that produces a luminosity spectrum that is almost indistinguishable from that of a Schwarzschild BH of the same mass as the DM core. (ii) The disc can enter deep inside the non-rotating DM core, allowing accretion-powered efficiencies of as high as 28%, which is comparable to that of a highly rotating Kerr BH.
Conclusions. These results, together with the existence of a critical DM core mass of collapse into a supermassive BH, open new avenues of research for two seemingly unrelated topics: AGN phenomenology and dark matter physics.

Key words. accretion, accretion disks – cosmology: miscellaneous – dark matter

1. Introduction

One of the central results of the Lambda cold dark matter (ΛCDM) standard cosmological model is the necessity to invoke a dark matter component in the composition of the Universe (Bahcall et al. 1999). However, how this component is distributed on inner galactic scales, and the precise nature and mass of the dark matter particles, are long-standing open questions (Bullock & Boylan-Kolchin 2017). A main available tool to tackle these questions is based on cosmological *N*-body (classical) simulations with adequate initial conditions; for example the ones provided by the ΛCDM paradigm (see e.g. Ivanov & Simonović 2020 and references therein). Although this paradigm provides a sound explanation as to the distribution of dark matter on large scales (>Mpc), it faces various challenges on short galactic scales (Diemand et al. 2005; Battaglia et al. 2008; Joung et al. 2009; Bullock & Boylan-Kolchin 2017).

Within the framework of cosmological simulations, different state-of-the-art alternatives are being provided in an attempt to solve these problems, including the possibility that cold DM is self-interacting (Kaplinghat & Ren 2020), considering warm instead of cold DM (Bozek et al. 2019), or even abandoning

the hypothesis of classical particles by incorporating quantum effects into the simulations (Schive et al. 2014). In an attempt to include the quantum nature of the DM particles explicitly in the physics of the DM halos, an alternative (semi-analytical) approach was recently proposed whereby fermionic DM is considered in a cosmological framework (Argüelles et al. 2021). This addresses the problems of DM halo formation, overall morphology, and stability from first principle physics. In particular, it includes (quantum) statistical mechanics and thermodynamics in the presence of self-gravity, offering solutions to some of the problems that the ΛCDM paradigm faces at short scales (see e.g. Krut et al. 2023; Argüelles & Becerra-Vergara 2023a for a recent work and a review, respectively).

Fermionic mass distributions of this sort are obtained by solving the equations of a self-gravitating system of neutral fermionic (spin 1/2) particles in hydrostatic and thermodynamic equilibrium in general relativity (GR). Some generic solutions to this model have been obtained by various authors aiming to address the problem of DM halos (Chau et al. 1984; Ingrosso & Ruffini 1988; Gao et al. 1990; Chavanis & Sommeria 1998; Bilic et al. 2002; Chavanis 2006; Destri et al. 2013; Argüelles & Ruffini 2014; Ruffini et al. 2015;

Chavanis et al. 2015), and just recently a more realistic version of this theory – including particle evaporation and central (fermion) degeneracy – was developed in GR by Argüelles et al. (2018, 2019, 2021) and is referred to here as the (extended) Ruffini-Argüelles-Rueda (RAR) model[1]. This model implies novel DM density profiles, which self-consistently account for the Pauli exclusion principle, yielding a source of quantum pressure towards the centre of the configurations with key implications for galactic nuclei. The more general DM profiles develop a 'dense core–diluted halo' morphology, which, unlike other phenomenological profiles in the literature, depends on the mass of the particle. Remarkably, these fermionic DM halos can explain the galaxy rotation curves in different galaxy types (Argüelles et al. 2018, 2019; Krut et al. 2023), while the degenerate fermion core can mimic their central BHs (Argüelles et al. 2018, 2019, 2022b,a, 2021; Becerra-Vergara et al. 2020; Becerra-Vergara & Argüelles 2021). Moreover, as demonstrated in Argüelles et al. (2021, 2023b,c) based on dynamical and thermodynamical stability criteria in GR, the central DM core can reach a critical mass for collapse and therefore provides a novel channel for supermassive BH formation in the early Universe (see also Chavanis & Alberti 2020; Alberti & Chavanis 2020 for a first dynamical and thermodynamical instability study in GR of the self-gravitating *Fermi* gas at finite temperature leading to BH formation).

In the present work, we centre our attention on fermionic core–halo profiles applied to typical active-like galaxies, together with their central accretion processes. Our study of the free parameters of the theory (including particle mass) focuses on solutions whose central core has not yet reached the critical mass for collapse, and therefore represents an alternative to the traditional BH scenario. This choice is motivated by our ambition to try to understand the very nature of the massive compact objects at the centres of galaxies, their formation channel, surrounding emission, and finally their relation with the host galaxy and AGN phenomenology.

Motivated by distinct branches of theoretical physics and astrophysics, different alternative models to that of the classical BHs have been proposed (see e.g. Cardoso & Pani 2019 for a review). When dealing with galaxy centres, a typical example studied in the recent past is the boson star (Schunck & Mielke 1999; Torres et al. 2000; Guzmán 2006; Vincent et al. 2016; Olivares et al. 2020), which is a horizonless and massive compact object made of self-gravitating scalar fields. In particular, the different observational signatures of boson stars have been studied, such as the luminosity spectra of α-discs (Guzmán 2006); strong-field images and luminosity patterns in boson stars surrounded by a disc torus (Vincent et al. 2016); and accretion flow via general relativistic magnetohydrodynamic simulations in the space-time of a boson star (Olivares et al. 2020).

In analogy to the above study cases, it is our objective to start a research program for AGN phenomenology dedicated to the RAR model for a self-gravitating system of fermions representing the DM in galaxies. In order to cover the main observational signatures associated with the emission of galaxy centres, we start in this work by studying the accretion of barionic matter onto supermassive compact cores made of fermionic DM, and the corresponding luminosity. To this end, we first extend the standard disc model of Shakura and Sunyaev (Shakura & Sunyaev 1973) in the presence of a fermionic DM

distribution using a Keplerian disc and a classical treatment. We are motivated to use fermionic particles because of the numerous efforts made in the last decade to shed light on the nature of such supermassive dark compact objects and the surrounding DM halo in a unified description (Argüelles & Becerra-Vergara 2023a).

The data coming from observational campaigns dedicated to the stellar motions around Sgr A* (Ghez et al. 2005, 2008; Genzel et al. 2010; GRAVITY Collaboration 2018) – confirming the presence of a supermassive compact object – have been used to show that the core–halo RAR solutions accurately reproduce the orbital motion of the S stars, including its relativistic effects (Becerra-Vergara et al. 2020; Becerra-Vergara & Argüelles 2021; Argüelles et al. 2022b). Additionally, observations of the relativistic images using Very Long Base Interferometry (VLBI) in both M87 and the Milky Way (The Event Horizon Telescope Collaboration 2019; Akiyama et al. 2022) can be used to further test the RAR solution, for which it is essential to study the accretion physics in this new paradigm.

The present article is organised as follows: We briefly describe our extended RAR model in Sect. 2. In Sect. 3, we study the efficiency, spectra, and solutions of steady-state thin discs that accrete in the background metric of the RAR model. Finally, in Sect. 4 we present the conclusions we derive from this work.

2. Model

2.1. Extended RAR solution

The RAR model consists in a spherical system of self-gravitating tempered fermions distributed in phase-space according to the following *Fermi*–Dirac-like distribution function:

$$f_c(\epsilon \leq \epsilon_c) = \frac{2}{h^3} \frac{1 - e^{(\epsilon - \epsilon_c)/kT}}{e^{(\epsilon - \mu)/kT} + 1}, \qquad f_c(\epsilon > \epsilon_c) = 0, \qquad (1)$$

where $\epsilon = \sqrt{c^2 p^2 + m^2 c^4} - mc^2$ is the particle kinetic energy, μ is the chemical potential with the particle rest-energy subtracted from it, T is the effective temperature, k is the Boltzmann constant, h is the Planck constant, c is the speed of light, and m is the fermion mass. Anti-fermions are not included as temperatures $T \ll mc^2/k$ are considered. The full set of (functional) dimensionless parameters of the model is made up of temperature, degeneracy, and cutoff parameters, $\beta = kT/(mc^2)$, $\theta = \mu/kT$, and $W = \epsilon_c/(kT)$, respectively.

Interestingly, a coarse-grained phase-space distribution of this kind can be linked with halo formation processes, because it can be obtained from a generalised kinetic theory in the presence of gravity as demonstrated in Chavanis (2004). Indeed, it was shown there that Eq. (1) is a (quasi-) stationary solution of a generalised Fokker-Planck equation for fermions (Chavanis 2004, 2006). Such a kinetic theory includes the physics of violent relaxation appropriate for non-linear structure formation – as originally presented in Lynden-Bell (1967) for classical particles –, though further extended to include particle evaporation and applied to realistic DM halos (Chavanis et al. 2015; Argüelles et al. 2021). This kind of phase-space distributions has been shown to fulfil a maximisation entropy principle during the collisionless relaxation process, until the halo reaches the steady state that is currently observed. More recently, this formation mechanism of fermionic halos was applied in Krut et al. (2023) to a sample of 120 galaxies, and compared

---

[1] The term 'relativistic fermionic King model' is also used in the literature (Chavanis 2022).

with phenomenological profiles as obtained from cosmological *N*-body simulations.

The corresponding four parametric fermionic equations of state at a given radius r, that is, $\rho(\beta, \theta, W, m)$, $P(\beta, \theta, W, m)$, are directly obtained as the corresponding integrals (bounded from above by $\epsilon \leq \epsilon_c$) of $f_c(p)$. These components are the diagonal part of the stress–energy tensor in the Einstein equations, which are solved under the perfect fluid approximation within a background metric with spherical symmetry, which reads

$$ds^2 = e^{\nu}c^2 dt^2 - e^{\lambda} dr^2 - r^2 d\Theta^2 - r^2 \sin^2 \Theta d\phi^2, \qquad (2)$$

where (r, Θ, ϕ) are the spherical coordinates, and ν and λ only depend on the radial coordinate r. The system of Einstein equations (i.e. the mass and the Tolman–Oppenheimer–Volkoff equations below) is solved together with the Tolman and Klein thermodynamic equilibrium conditions (involved in Eqs. (5)–(6) below), and (particle) energy conservation along a geodesic (Eq. (7) below). The dimensionless system of highly non-linear ordinary differential equations reads:

$$\frac{d\hat{M}_{DM}}{d\hat{r}} = 4\pi \hat{r}^2 \hat{\rho}, \qquad (3)$$

$$\frac{d\nu}{d\hat{r}} = \frac{2(\hat{M}_{DM} + 4\pi \hat{P}\hat{r}^3)}{\hat{r}^2(1 - 2\hat{M}_{DM}/\hat{r})}, \qquad (4)$$

$$\frac{d\theta}{d\hat{r}} = -\frac{1 - \beta_0(\theta - \theta_0)}{\beta_0} \frac{\hat{M}_{DM} + 4\pi \hat{P}\hat{r}^3}{\hat{r}^2(1 - 2\hat{M}_{DM}/\hat{r})}, \qquad (5)$$

$$\beta(\hat{r}) = \beta_0 e^{\frac{\nu_0 - \nu(\hat{r})}{2}}, \qquad (6)$$

$$W(\hat{r}) = W_0 + \theta(\hat{r}) - \theta_0, \qquad (7)$$

where the dimensionless quantities are: $\hat{r} = r/\chi$, $\hat{M}_{DM} = GM_{DM}/(c^2\chi)$, $\hat{\rho} = G\chi^2\rho/c^2$, $\hat{P} = G\chi^2 P/c^4$, with $\chi = 2\pi^{3/2}(\hbar/(mc))(m_p/m)$ and $m_p = \sqrt{\hbar c/G}$ the Planck mass. The system of Eqs. (3)–(7) constitutes a boundary condition problem, which, for fixed DM particle mass m, has to be solved for a given set of free parameters (β_0, θ_0, W_0) defined at the centre of the configuration.

The most general solution results in a degenerate compact core (governed by Pauli degeneracy pressure) surrounded by an extended and more diluted halo (governed by thermal pressure) as detailed in the following section and in Argüelles et al. (2018). The core mass $M_c = M_{DM}(r_c)$ is given at the core radius, which is defined as the first maximum of the rotation curve. This latter corresponds to the radius where the central density has decreased by about one-tenth of the central value, which is where fermion degeneracy starts to vanish. In the following section, we show different solutions for well-motivated values of m, with DM core masses and total halo masses typical of active-like galaxies, following Argüelles et al. (2019).

2.2. Application to active-like galaxies

The application of the extended RAR model to large galaxies with dark and regular compact cores reaching mass values of $\sim 10^7 - 10^8 \, M_{\odot}$ typical of AGN was first shown in Argüelles et al. (2019). This was done for a DM particle mass of $m \approx 50$ keV, which was motivated by the excellent results obtained for the Milky Way (Argüelles et al. 2018, 2022b; Becerra-Vergara et al. 2020; Becerra-Vergara & Argüelles 2021), where the corresponding DM core explains the motion of the S-cluster stars around SgrA*. For a similar value of fermion mass,
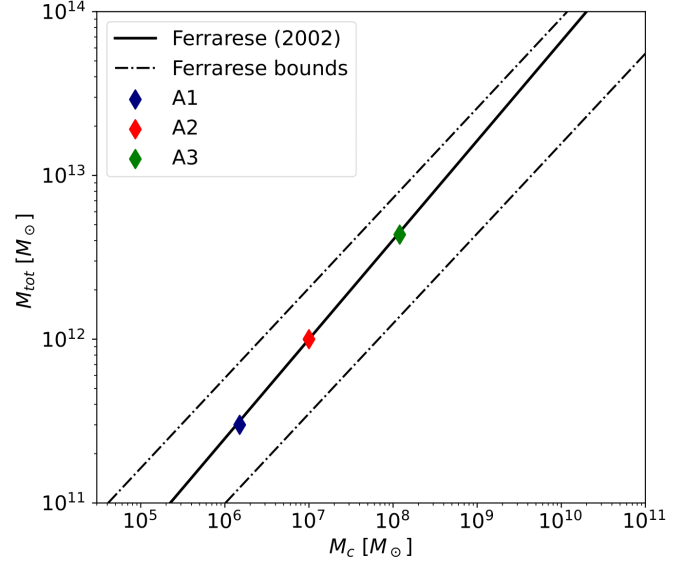
Fig. 1. Core–halo RAR solutions for DM particle mass of $mc^2 = 48$ keV, in agreement with the Ferrarese relation connecting the halo mass with the supermassive central object mass (Ferrarese 2002).

the highly degenerate core reaches the critical mass of collapse M_c^{cr} into a supermassive black hole (SMBH) of $\approx 2 \times 10^8 \, M_{\odot}$ (Argüelles et al. 2021). Particle masses of the order of $\sim 100 - 350$ keV have also been analysed within this DM model with excellent results (see e.g., Argüelles et al. 2018, 2023b). As demonstrated in Argüelles & Ruffini (2014) and Argüelles et al. (2021), the larger the m, the lower the critical core masses $M_c^{cr} \approx M_{OV} \propto 1/m^2$ (roughly following the Oppenheimer-Volkoff limit; Oppenheimer & Volkoff 1939), with $m \approx 350$ keV leading to a critical mass of a DM core collapsing to a SMBH of $\approx 4 \times 10^6 \, M_{\odot}$ as for SgrA* (Argüelles et al. 2018; Becerra-Vergara et al. 2020).

An important result of the core–halo family of RAR DM profiles for given m, is that it follows different universal scaling relations, such as: the Ferrarese relation (Ferrarese 2002; Bogdán & Goulding 2015), which connects the halo and its supermassive central object masses; the DM surface density relation (Donato et al. 2009), and the radial acceleration relation (McGaugh & Lelli 2016), as shown in Argüelles et al. (2019), Krut et al. (2023). Indeed, in Fig. 1 we show an example of RAR profiles with $m = 48$ keV (solutions $A1 - A3$), corresponding to a halo mass window of $M_{tot} \sim 10^{11} - 10^{12} \, M_{\odot}$ and supermassive DM compact objects of masses of $M_c \sim 10^6 - 10^8 \, M_{\odot}$, in excellent agreement with the Ferrarese relation (RAR models with $m = 200$ keV are also in agreement with the correlation, though reach up to $M_c \sim 10^7 \, M_{\odot}$).

One of the central objectives of this work is to analyse the accretion power efficiencies and consequent luminosity spectrum caused by supermassive compact objects alternative to BHs. Due to the fact that larger fermion masses imply more compact and denser DM cores at a given core mass (see e.g. Argüelles et al. 2018), we study two different families of profiles here: those with $mc^2 = 48$ keV (which we call RAR model A), and those with $mc^2 = 200$ keV (RAR model B). Table 1 shows the main parameters of the two models: for a typical DM compact-core mass of $10^7 \, M_{\odot}$, model B2 gives a more compact core than the A2 solution (see Fig. 2 for a comparison of the two profiles). The DM core mass in solution B2 is close to the critical mass of gravitational collapse to a Schwarzschild BH

Table 1. Main parameters of the different RAR models.

Model	Particle mass [keV]	M_c [$M_\odot$]	M_{tot} [$10^{11} M_\odot$]	r_c [r_g]	θ_0	W_0	β_0
A1	48	1.5×10^6	3	1.5×10^4	39.5	69.6	2.5×10^{-6}
A2	48	1.0×10^7	10	1.0×10^3	37.9	66.6	6.8×10^{-5}
A3	48	1.2×10^8	45	3.4×10^1	38.8	67.2	1.1×10^{-3}
B1	200	3.5×10^6	3	8.1×10^1	49.4	77.9	5.1×10^{-3}
B2	200	1.0×10^7	10	1.5×10^1	44.3	75.4	2.1×10^{-3}
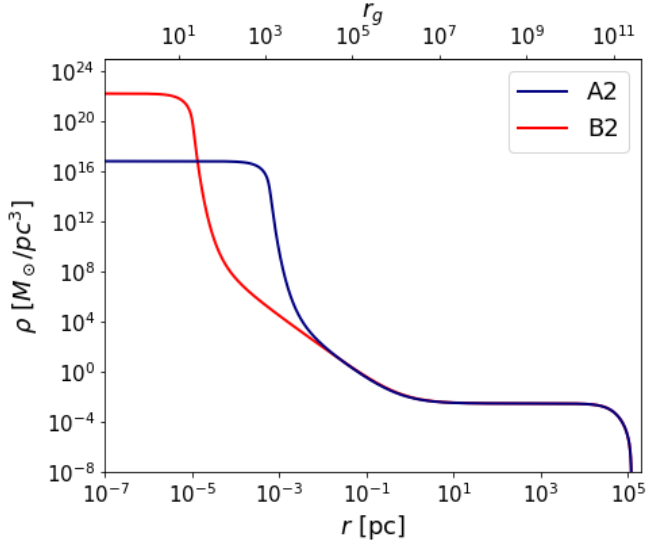
Fig. 2. Density profiles corresponding to a core mass of $M_c = 1.0 \times 10^7 M_\odot$, and particle masses of $mc^2 = 48$ keV (A2, blue) and $mc^2 = 200$ keV (B2, red). These DM halos correspond to typical Elliptical galaxies.

Fig. 3. Metric components corresponding to the same RAR solutions as in Fig. 2 but with a core mass of $M_c = 10^7 M_\odot$, and particle masses of $mc^2 = 48$ keV (A2, blue) and $mc^2 = 200$ keV (B2, red). A comparison with the metric of a Schwarzschild BH of mass $M_{BH} = 10^7 M_\odot$ is also shown (BH, green).
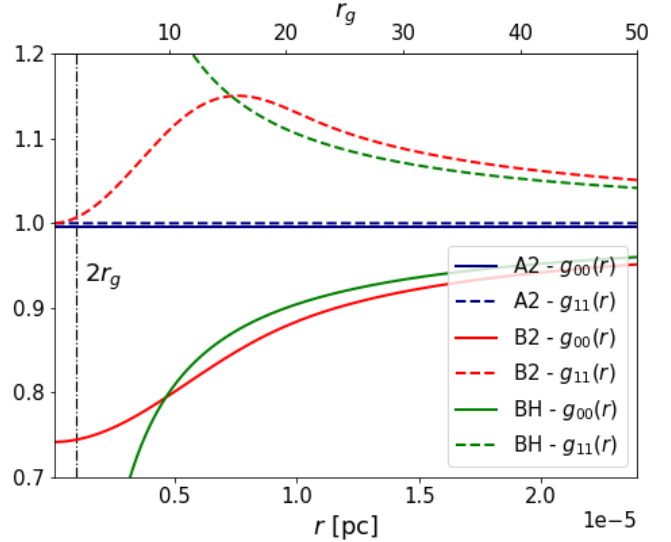
of that mass and therefore implies very similar metric functions (see Fig. 3).

Figure 2 shows the density profiles for models A2 and B2. These clearly demonstrate the existence of compact and massive cores corresponding to the highest density trends, and the diluted halo at larger radii. This is because the system goes from being governed by fermionic degeneracy pressure at small radii to be governed by thermal pressure at larger radii. The density profile therefore transitions from a degenerate core of almost constant density to a Boltzmann-like regime in the outer halo, where the density falls off as a power law followed by an exponential decrease determining the galaxy border.

3. Accretion discs

3.1. Efficiency

There is an essential difference between the Schwarzschild BH solution and the RAR DM model regarding the motion of massive particles in their surroundings. Because the former is a singular solution of the Einstein equations and the latter is not, the existence of the innermost stable circular orbit (ISCO) becomes discernable. Due to the regularity of the central object in the RAR case, there is no critical angular momentum of the particle for which a potential barrier is no longer present, and therefore no ISCO can be reached (Crespi 2022). This behaviour directly

implies that the disc has no clear inner boundary[2]. To set an inner constraint in this regard, we study the binding energy of a test particle in the disc, and analyse when it saturates towards a maximum.

In the case of BHs, the efficiency of the accretion process is related to the binding energy per unit rest mass at the innermost stable circular orbit (ISCO), that is:

$$\varepsilon = \frac{mc^2 - E_c}{mc^2}, \qquad (8)$$

where E_c corresponds to the particle's energy at the last stable circular orbit. This accretion efficiency represents the maximum fraction of the rest mass energy of the accreted particle that can be converted into radiated energy. In standard astrophysical scenarios such as a neutron star of radius ~ 10 km, the efficiency is of the order of 10%, while in the case of BH accretion the efficiency varies between 5.7% and 42% for Schwarzschild and Kerr (maximal rotation with a prograde disc) solutions, respectively[3]

---

[2] General relativistic simulations of fluid dynamics should be performed to tackle this problem in analogy to boson stars either for unmagnetised (Meliani et al. 2016) or magnetised scenarios (Olivares et al. 2020), though both are out of the scope of this paper.
[3] When considering the effects of the radiation of the disc on the rotation of the black hole, the maximum spin reduces, and the efficiency results in 32.4% (Thorne 1974; Laor & Netzer 1989).

(Novikov et al. 1973). In analogy to the BH case, and in order to define the corresponding accretion efficiency in the RAR model, we seek a maximum in the radial behaviour of the (normalised) binding energy of a test particle. Therefore, in the RAR solution, the binding energy normalised to the rest mass reads

$$\bar{E}_b(r) = 1 - \sqrt{g_{00}(r)\left(1 + \frac{r g'_{00}(r)}{2g_{00}(r) - r g'_{00}(r)}\right)}, \qquad (9)$$

where $g_{00}(r) = e^{\nu(r)}$ is the temporal component of the metric, and the prime symbol indicates derivation with respect to r. We show this binding energy behaviour in Fig. 4 for the case of a Schwarzschild BH obtained by replacing $g_{00}(r)$ in Eq. (9) by $1 - 2GM/r$-, and for two different RAR solutions with the same DM core mass of $M_c = M_{BH} = 10^7 M_\odot$ but different core compacities. For the RAR solutions, the binding energy asymptotically reaches the maximum as $r \to 0$, and saturates (see definition below) at a given radius r_{in}. The definition for r_{in} implies that it is always smaller than the core radius, with the binding energy remaining approximately constant as the particle's orbit gets smaller and smaller (i.e. until $r_{min} \sim 10^{-7} r_g \approx 10^{-13}$ pc, the smallest representable radius admitted by computer precision for such core–halo solutions). As the inner radius of the disc, r_{in}, we adopt the value at which the relative error for the change in the maximum efficiency of the binding energy is equal to or lower than 1%, that is

$$\frac{|\bar{E}_b(r_{in}) - \bar{E}_b(r_{min})|}{\bar{E}_b(r_{min})} \leq 0.01. \qquad (10)$$

Adopting this definition, the inner radius typically corresponds to one-tenth of the core radius $r_{in} \sim 0.1 r_c$ (for 1% of relative error). In Table 2, we list the values of the inner radius and efficiency for the different RAR models. We compare the efficiencies of the RAR models A_2 and B_2 (labelled ε_{A2} and ε_{B2} in Fig. 4) with the Schwarzschild efficiency labelled ε_{BH}. Remarkably, as the disc can enter deep inside the DM core (i.e. the Keplerian orbits in the disc can have $r < r_c$), the binding energy of RAR solutions with sufficiently compact cores can surpass the maximum Schwarzschild value. Figure 4 shows an example of a subcritical DM core (solution B_2) with an efficiency of 14%, to be compared with the 5.7% of the BH case. Moreover, when the degenerate core achieves its critical mass of collapse, the accretion efficiency can be as large as ≈28%, which is similar to that of a highly rotating Kerr BH. This interesting result is not new, and analogous conclusions were obtained for relativistic clusters with constant density and different compacities by Cocco et al. (1995).

These results, exemplified in Fig. 4, have potential implications for the astrophysics of AGNs. In the context of the Soltan argument (Soltan 1982), and based on observational results regarding the mean accretion efficiency of SMBHs (both from the local and the AGN-relic Universe; Yu & Tremaine 2002; Ueda et al. 2003; Marconi et al. 2004), a mean value of $\epsilon \approx 0.1$ arises, which falls between that predicted by the Schwarzschild and Kerr BH cases. Additionally, a data analysis of different populations of AGNs showed that the required efficiencies are $\epsilon > 0.1$ (Raimundo & Fabian 2009), with the majority of cases exhibiting $\epsilon \sim 0.2$-0.3 and the minority reaching down to as low as 0.04 (such low values are compatible with the findings of Marconi et al. 2004). Given these values, the relevance of the results presented here for the accretion efficiencies onto the compact DM cores becomes clear: depending on the compacity of the fermion core, the efficiency can go from below the typical Schwarzschild case up to values of larger than 0.1, which is
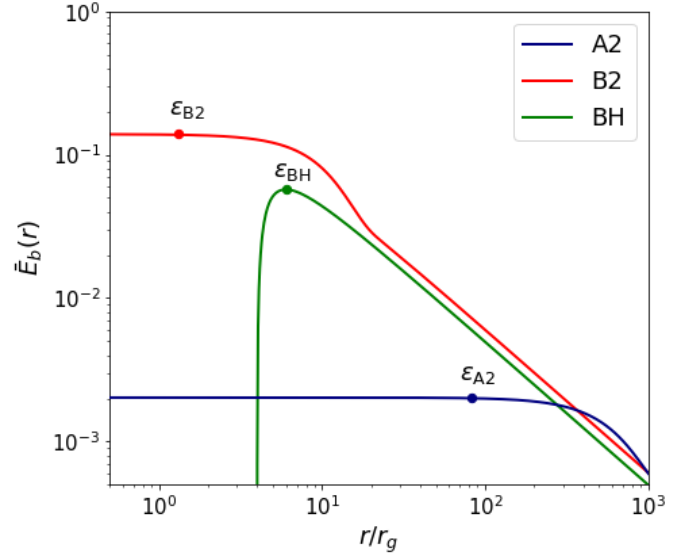
Fig. 4. Accretion efficiencies (labelled with coloured dots) for two different DM core compacies (i.e. different m) with the same core mass of $M_c = 10^7 M_\odot$ (RAR solutions A_2 and B_2). For comparison, the case of a Schwarzschild BH with a mass equal to M_c is also shown. Interestingly, solution B_2 reaches an accretion efficiency of 14%, which is considerably larger than that of the Schwarzschild BH.

typical of Kerr BHs. Further discussions about the challenges faced in observationally confirming the Kerr BH space-time at galaxy centres – which are mainly related to degeneracy in models regarding the mass of the compact object, and in particular the spin parameter and possible deviations from the Kerr metric – can be found in Bambi (2017).

3.2. The steady standard disc model embedded in DM

In this section, we consider the model of steady thin discs developed by (Shakura & Sunyaev 1973), and extend it to be applied in the context of RAR solutions. To this end, and following the treatment presented in Frank et al. (2002), we use cylindrical polar coordinates (r, ϕ, z), and assume that matter is very close to the plane $z = 0$, and is rotating with an angular velocity $\Omega(r)$ that remains very close to the Keplerian value:

$$\Omega = \Omega_K(r) = \left(\frac{GM(r)}{r^3}\right)^{1/2}. \qquad (11)$$

Here, $M(r)$ is the mass distribution of the DM core–halo solution contained up to r. The circular velocity is given by $v_\phi = r\Omega_K(r)$.

In addition, the gas is assumed to possess a small radial 'drift' velocity $v_R(r)$, which is negative near the central object so that matter is accreted. The disc is characterised by its surface density $\Sigma(r)$, which is the mass per unit surface area of the disc, given by integrating the gas density ρ in the z-direction. For a steady disc, the conservation of mass and angular momentum can be written as:

$$\dot{M} = 2\pi r \Sigma(-v_R), \qquad (12)$$

$$\eta\Sigma = \frac{\dot{M}}{3\pi}\left[1 - \left(\frac{M_{in} r_{in}}{M(r) r}\right)^{1/2}\right]\left[1 - \frac{r}{3M(r)}\frac{dM(r)}{dr}\right]^{-1}, \qquad (13)$$

respectively. Here, $\dot{M}$ is the accretion rate (in units of g s^{-1}), η is the cinematic viscosity, r_{in} is the internal radius of the disc (see Sect. 3.1), and $M_{in} = M(r_{in})$.

Table 2. r_{in} considered for the different models.

Model	Particle mass [keV]	M_c [$M_\odot$]	r_c [r_g]	r_{in} [r_g]	ε [%]
A1	48	1.5×10^6	1.5×10^4	9.6×10^2	0.02
A2	48	1.0×10^7	1.0×10^3	8.3×10^1	0.2
A3	48	1.2×10^8	3.4×10^1	2.6×10^0	6.7
B1	200	3.5×10^6	8.1×10^1	6.8×10^0	2.5
B2	200	1.0×10^7	1.5×10^1	1.3×10^0	14
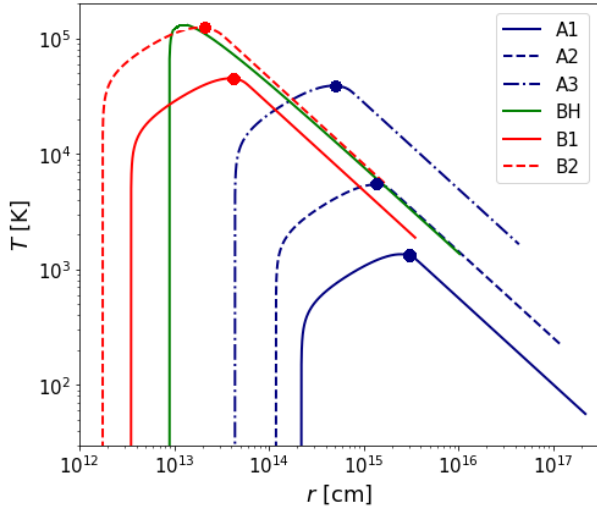
Fig. 5. Comparison of disc temperatures for the A and B RAR models with that of a BH with a mass of $M_{BH} \sim 10^7 \, M_\odot$. The dots indicate the location of the R_c for each RAR model.

In analogy to the BH case, we engineer the viscous torques to vanish at the maximum of the binding energy, which in the case of the RAR model corresponds to the inner radius r_{in}. This allows us to explicitly obtain the viscous dissipation per unit disc face area, as

$$D(r) = \frac{1}{2}\eta\Sigma\left(r\frac{d\Omega}{dr}\right)^2$$
$$= \frac{3\dot{M}}{8\pi}\frac{GM(r)}{r^3}\left[1 - \left(\frac{M_{in}r_{in}}{M(r)r}\right)^{1/2}\right]\left[1 - \frac{r}{3M(r)}\frac{dM(r)}{dr}\right]. \quad (14)$$
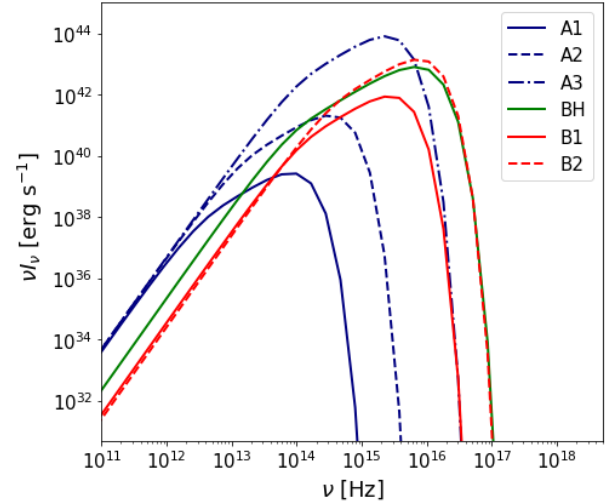
It can be seen that, as in the standard solution, the viscous dissipation is independent of the physical nature of the viscosity η. Finally, the total disc luminosity is obtained by integrating $D(r)$ along the disc area.

We also consider an optically thick disc in the z-direction, and therefore each element of the disc radiates as a black body with temperature $T(r)$, given by the equation of the viscous dissipation per unit disc face area $D(r) = \sigma T^4(r)$, where σ is the Stefan-Boltzmann constant. Figure 5 shows a comparison between the A and B RAR models and a BH of $M \sim 10^7 \, M_\odot$.

For an observer at a distance d from the centre of the disc, whose line of sight makes an angle i with respect to the normal of the disc plane, the flux at frequency ν is

$$F_\nu = \frac{4\pi h \cos i \nu^3}{c^2 d^2}\int_{r_{in}}^{r_{out}}\frac{r dr}{e^{h\nu/kT(r)} - 1}. \quad (15)$$

The outer radius r_{out} can be estimated using the condition that the disc becomes locally self-gravitating

(Bogdán & Goulding 2015). This is determined by analysing the stability criterion for a differential rotation disc:

$$Q_T = c_S\Omega/\pi G\Sigma \gg 1, \quad (16)$$

where Ω is the angular velocity given in Eq. (11). The condition $Q_T = 1$ defines the self-gravitating disc:

$$r_{out} = (M/\pi\rho)^{1/3}. \quad (17)$$

Knowing the density of the accretion disc, the outer radius can be determined. Further details are discussed in Appendix A, where we obtain $r_{out} \approx 10^3 \, r_g - 10^4 \, r_g$, depending on the model studied. Nevertheless, the disc beyond $10^3 \, r_g$ does not contribute significantly to the total luminosity, and therefore we adopt this value as the outer limit for all models.

Figure 6 shows the luminosities obtained for models A and B. In all cases, we consider $\dot{M} = 0.1\dot{M}_{Edd}$, where $\dot{M}_{Edd}$ is the Eddington accretion rate, defined as the accretion rate at which the compact source radiates at an efficiency of $\epsilon \sim 0.1$ of the Eddington luminosity, that is $\dot{M}_{Edd} = L_{Edd}/\epsilon c^2 \sim 1.4 \times 10^{16}(M_c/M_\odot) \, \text{erg s}^{-1}$. Moreover, we show the comparison with a black hole of $M \sim 10^7 \, M_\odot$. See also points (ii) and (iii) in Sect. 4 for a relevant discussion regarding the RAR model predictions for disc luminosities.

Figure 7 only shows the luminosity for RAR models with $M_c = 10^7 \, M_\odot$, using two values for the fermion mass: $mc^2 = 48 \, \text{keV}$ (model A2) and $mc^2 = 200 \, \text{keV}$ (model B2); we also compare this result with a disc around a Schwarzschild BH of $M_{BH} = M_c$. This important result shows that a core compacity (i.e. solution B2) exists at which the luminosity spectrum is

Fig. 6. Comparison of the luminosity for the A and B models with a BH of $M \sim 10^7 \, M_\odot$.
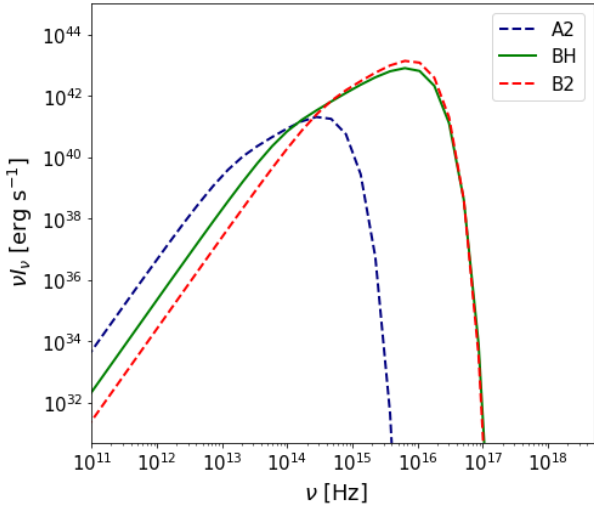
Fig. 7. Comparison of the luminosity in the A2 and B2 models and that of a BH of $\sim 10^7 \, M_\odot$.
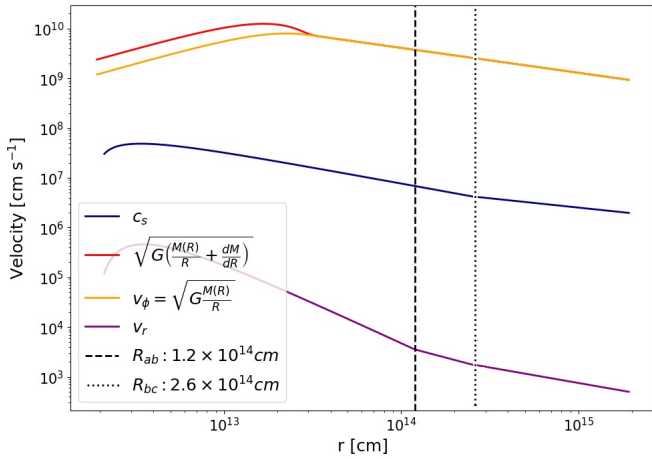
Fig. 8. Hypothesis validation for model A2: Keplerian velocity must be highly supersonic, while radial velocity must be highly subsonic. Vertical dashed (and doted) lines specify R_{ab} (and R_{bc}), i.e. the radii at which the behaviour of the disc changes between the inner and intermediate region (and between the intermediate and outer region), respectively (see Appendix A).

almost indistinguishable from that of a Schwarzschild BH of the same mass as the DM core.

In the standard thin disc model, different hypotheses are considered: the azimuthal velocity v_ϕ remains close to the Keplerian value; the disc remains thin at all radii (i.e. the height scale H is much smaller than the extent of the disc $H \ll r$); and the disc is optically thick in the z-direction. In order to verify that the solutions here obtained for the RAR model are consistent with the above thin disc ansatz, we consider a disc in hydrostatic equilibrium in the z-direction, meaning that there is no flow in the vertical direction. Then, for $H \ll r$ and $P \approx \rho c_s^2$ (with c_s the sound speed), the solution satisfies:

$$c_s \ll \left(\frac{GM(r)}{r} + G\frac{dM(r)}{dr} \right)^{1/2} \approx \left(\frac{GM(r)}{r} \right)^{1/2}. \tag{18}$$

The local standard Kepler velocity should be highly supersonic.

If the thin disc condition in Eq. (18) holds, the circular matter velocity v_ϕ satisfies

$$v_\phi = \sqrt{\frac{GM(r)}{r} + G\frac{dM(r)}{dr}}[1 + O(M^{-2})]. \tag{19}$$

It can be seen that v_ϕ is very close to the Keplerian value, as assumed above. Figure 8 shows both hypotheses for model A2 as an example; though it is satisfied by all solutions, as we have verified.

At this point, it is worth emphasising that the complete structure of the disc is not needed in order to compute the spectra for the RAR solutions. However, in order to be able to verify the hypothesis mentioned above, in Appendix A we write out the generalisation of the Shakura & Sunyaev set of equations within the fermionic DM model, and solve for the complete disc structure within the α prescription of the viscosity (see Frank et al. 2002 in order to make the analogous demonstration in the case of the standard α disc theory).

4. Discussion and final remarks

We extended the standard, steady thin disc model in order to study the accretion onto horizonless dark compact objects at the centres of galaxies. The BH alternative investigated here consists in a dense and highly degenerate core made of neutral fermions, surrounded by a more diluted mass distribution that is able to explain the DM halo in galaxies. This dense core–diluted halo DM configuration is known as the RAR model, and is a non-analytic solution of the Einstein equations of GR, which naturally arises once the quantum nature (i.e. Pauli principle) of the fermions is duly accounted for. The attention in this work is focused on active-like galaxies together with their central accretion processes, luminosity spectra, and efficiencies.

We used core–halo RAR solutions for two different fermion masses, 48 keV and 200 keV, the latter corresponding to a very dense DM core with a mass of $10^7 \, M_\odot$, close to its critical value of gravitational collapse to a BH. The fact that, as m increases, the DM-core of given mass becomes more compact (see Fig. 2) makes the above choice particularly relevant to the analysis of how similar the luminosity spectra of α-discs can be to those of a BHs. Moreover, a particle mass falling within this range is totally compatible with both linear structure formation in cosmology and non-linear structure formation, including galaxy rotation curves and scaling relations (see Argüelles & Becerra-Vergara 2023a for a review and references therein).

The main results of our work can be summarised as follows:

1. The fact that the dense DM core is transparent implies that the accretion disc can enter inside reaching down to event-horizon scales. As a consequence, it can achieve accretion efficiencies of as large as $\epsilon = 28.5\%$, which is comparable to that of a highly rotating Kerr BH. Figure 4 shows a relevant example comparing a $10^7 \, M_\odot$ Schwarzschild BH with two different RAR solutions of increasing particle mass (A_2 and B_2) with the same core mass. We show that for $m = 48$ keV (solution A_2) the efficiency is below 1% while for $m = 200$ keV (solution B_2), the stable (i.e. below critical) DM core is compact enough to reach an accretion efficiency at $r_{in} < r_c$ that is more than two times that of the BH. The maximum efficiency of $\epsilon = 28.5\%$ is achieved for the critical core mass. The relevance of achieving Kerr-like efficiencies in active galaxies is supported by observational results (Raimundo & Fabian 2009) based on the Soltan argument.

2. At a given DM core mass M_c, the larger the particle mass, the more compact the degenerate core, and consequently the more luminous and energetic the discs. This result, when considered in light of the efficiency trend explained above, implies that there always exists a given core compacity at which the luminosity spectrum is almost indistinguishable from that of a Schwarzschild BH of the same mass as the DM core. This important RAR model prediction is explicitly shown in Fig. 7 for a BH mass of $10^7 \, M_\odot$, which is typical of an active galaxy.

3. At fixed DM particle mass, it is possible to have different DM core masses M_c (see Table 1) with surrounding DM halos fulfilling the observationally inferred Ferrarese scaling relation (Ferrarese 2002; see Fig. 1 and Argüelles et al. 2019). A novel RAR model prediction found in this work is that when M_c increases, the peak frequency of the luminosity spectra also increases (see e.g. the trend in the red curves B_1 and B_2 of Fig. 6). This is due to the degeneracy of the core, which implies more compact solutions for more massive cores (at given m). This result is at odds with what is expected from accretion onto a BH, and could be a fundamental tool for testing the RAR model (see discussion below).

Further detailed work is needed in order to differentiate the two above paradigms of supermassive compact objects; for example making use of real spectral energy distributions (SED) of AGNs, or calculating the relativistic images produced by the emitted photons via ray-tracing techniques. The latter is an important project that has already been started by our team, and will allow us to compare observations of the shadow-like features predicted by the RAR model with those predicted by the BH.

Regarding the observational access to SEDs of AGNs relative to this work, the most important is the narrow window of low central-object masses of $\sim 10^6 - 10^7 \, M_\odot$ (for the $m = 200 \, \text{keV}$ case), or $\sim 10^7 - 10^8 \, M_\odot$ (for $m = 48 \, \text{keV}$), before the corresponding DM core becomes critical and collapses to a BH[4]. An eventual observational detection of the luminosity peaks that shift towards higher ν in such a small DM core-mass window is challenging. This is mainly because of the lack of data in the UV band (at about the UV bump) due to the absorption of the IGM; the large error bars at the blue bump; or the fact that most of the observed SEDs are obtained for relatively large central object masses, that is, of $>10^8 \, M_\odot$ (Collinson et al. 2017).

In summary, the original results presented in this work and summarised above may imply an important landmark – and may open new avenues of research – in the field of AGN theory and phenomenology in connection to DM physics and SMBHs.

References

Akiyama, K., Alberdi, A., Alef, W., et al. 2022, ApJ, 930, L13
Alberti, G., & Chavanis, P.-H. 2020, Eur. Phys. J. B, 93, 208
Argüelles, C. R., & Ruffini, R. 2014, Int. J. Mod. Phys. D, 23, 1442020
Argüelles, C. R., Krut, A., Rueda, J. A., & Ruffini, R. 2018, Phys. Dark Univ., 21, 82

Argüelles, C. R., Krut, A., Rueda, J. A., & Ruffini, R. 2019, Phys. Dark Univ., 24, 100278
Argüelles, C. R., Díaz, M. I., Krut, A., & Yunis, R. 2021, MNRAS, 502, 4227
Argüelles, C. R., Becerra-Vergara, E. A., Krut, A., et al. 2022a, Int. J. Mod. Phys. D, 31, 2230002
Argüelles, C. R., Mestre, M. F., Becerra-Vergara, E. A., et al. 2022b, MNRAS, 511, L35
Argüelles, C. R., Becerra-Vergara, E. A., et al. 2023a, Universe, 9, 197
Argüelles, C. R., Boshkayev, K., Krut, A., et al. 2023b, MNRAS, 523, 2209
Argüelles, C. R., Rueda, J. A., & Ruffini, R., 2023c ApJ, submitted [arXiv:2312.07461]
Bahcall, N. A., Ostriker, J. P., Perlmutter, S., & Steinhardt, P. J., 1999, Science, 284, 1481
Bambi, C. 2017, Rev. Mod. Phys., 89, 025001
Battaglia, G., Helmi, A., Tolstoy, E., et al. 2008, ApJ, 681, L13
Becerra-Vergara, E. A., Argüelles, C. R., Krut, A., et al. 2020, A&A, 641, A34
Becerra-Vergara, E. A., Argüelles, C. R., et al. 2021, MNRAS, 505, L64
Bilic, N., Munyaneza, F., Tupper, G. B., & Viollier, R. D. 2002, Prog. Part. Nucl. Phys., 48, 291
Bogdán, A., & Goulding, A. D. 2015, ApJ, 800, 124
Bozek, B., Fitts, A., Boylan-Kolchin, M., et al. 2019, MNRAS, 483, 4086
Bullock, J. S., & Boylan-Kolchin, M. 2017, ARA&A, 55, 343
Cardoso, V., & Pani, P. 2019, Liv. Rev. Relativ., 22, 4
Chau, W. Y., Lake, K., & Stone, J. 1984, ApJ, 281, 560
Chavanis, P.-H. 2004, Phys. A Stat. Mech. Appl., 332, 89
Chavanis, P. H. 2006, Int. J. Mod. Phys. B, 20, 3113
Chavanis, P.-H. 2022, Phys. Rev. D, 106, 043538
Chavanis, P.-H., & Alberti, G. 2020, Phys. Lett. B, 801, 135155
Chavanis, P. H., & Sommeria, J. 1998, MNRAS, 296, 569
Chavanis, P.-H., Lemou, M., & Méhats, F. 2015, Phys. Rev. D, 92, 123527
Cocco, V., Pascale, E., & Ruffini, R. 1995, Nuovo Cimento B Serie, 110B, 95
Collinson, J. S., Ward, M. J., Landt, H., et al. 2017, MNRAS, 465, 358
Crespi, V. 2022, M.sc. Thesis, UNLP. Universidad Nacional de La Plata, Argentina
Destri, C., de Vega, H. J., & Sanchez, N. G. 2013, New Astron., 22, 39
Diemand, J., Zemp, M., Moore, B., Stadel, J., et al. 2005, MNRAS, 364, 665
Donato, F., Gentile, G., Salucci, P., et al. 2009, MNRAS, 397, 1169
Ferrarese, L. 2002, ApJ, 578, 90
Frank, J., King, A., & Raine, D. J. 2002, Accretion Power in Astrophysics: Third Edition (Cambridge, UK: Cambridge University Press)
Gao, J. G., Merafina, M., & Ruffini, R. 1990, A&A, 235, 1
Genzel, R., Eisenhauer, F., & Gillessen, S. 2010, Rev. Mod. Phys., 82, 3121
Ghez, A. M., Salim, S., Hornstein, S. D., et al. 2005, ApJ, 620, 744
Ghez, A. M., Salim, S., Weinberg, N. N., et al. 2008, ApJ, 689, 1044
GRAVITY Collaboration (Abuter, R., et al.) 2018, A&A, 618, L10
Guzmán, F. S. 2006, Phys. Rev. D, 73, 021501
Ingrosso, G., & Ruffini, R. 1988, Nuovo Cimento B Serie, 101, 369
Ivanov, M. M., Simonović, M., et al. 2020, Phys. Rev. D, 101, 083504
Joung, M. R., Cen, R., & Bryan, G. L. 2009, ApJ, 692, L1
Kaplinghat, M., Ren, T., et al. 2020, J. Cosmol. Astropart. Phys., 2020, 027
Krut, A., Argüelles, C. R., Chavanis, P. H., et al. 2023, ApJ, 945, 1
Laor, A., & Netzer, H. 1989, MNRAS, 238, 897
Lynden-Bell, D. 1967, MNRAS, 136, 101
Marconi, A., Risaliti, G., Gilli, R., et al. 2004, MNRAS, 351, 169
McGaugh, S. S., Lelli, F., et al. 2016, Phys. Rev. Lett., 117, 201101
Meliani, Z., Grandclément, P., Casse, F., et al. 2016, Class. Quant. Grav., 33, 155010
Novikov, I. D., & Thorne, K. S. 1973, in Black Holes (Les Astres Occlus), eds. C. Dewitt, & B. S. Dewitt, 343
Olivares, H., Younsi, Z., Fromm, C. M., et al. 2020, MNRAS, 497, 521
Oppenheimer, J. R., & Volkoff, G. M. 1939, Phys. Rev., 55, 374
Raimundo, S. I., & Fabian, A. C. 2009, MNRAS, 396, 1217
Ruffini, R., Argüelles, C. R., & Rueda, J. A. 2015, MNRAS, 451, 622
Schive, H.-Y., Chiueh, T., & Broadhurst, T. 2014, Nat. Phys., 10, 496
Schunck, F. E., & Mielke, E. W. 1999, GR and Gravitation, 31, 787
Shakura, N. I., & Sunyaev, R. A. 1973, A&A, 24, 337
Soltan, A. 1982, MNRAS, 200, 115
Thorne, K. S. 1974, ApJ, 191, 507
The Event Horizon Telescope Collaboration (Akiyama, K., et al.) 2019, ApJ, 875, L1
Torres, D. F., Capozziello, S., & Lambiase, G. 2000, Phys. Rev. D, 62, 104012
Ueda, Y., Akiyama, M., Ohta, K., & Miyaji, T. 2003, ApJ, 598, 886
Vincent, F. H., Meliani, Z., Grandclément, P., Gourgoulhon, E., & Straub, O. 2016, Class. Quant. Grav., 33, 105015
Yu, Q., & Tremaine, S. 2002, MNRAS, 335, 965

---

[4] Once the SMBH is formed from DM core collapse, it will grow further via baryonic accretion (Argüelles et al. 2023b) and show the standard spectral energy features.

Appendix A: Local structure of the disc

Here, we present the solution of the complete disc structure. To this end, we consider, as in the standard disc solution, the $\alpha-$ prescription for the viscosity, given by:

$$\eta = \alpha c_s H. \tag{A.1}$$

The following theoretical content of this Appendix is provided both for completeness and in order to be able to verify the three main hypotheses of the (extended) Shakura & Sunyaev theory: the geometrically thin disc ($H(r) << r$) and the Keplerian velocity approximation, together with the optically thick ($\tau > 1$) assumption, for which the solution of the full disc structure is needed. An example of such a verification is shown in Fig. 8 of the main text.

In the thin disc approximation, the determination of the disc structure is simplified. Following Shakura & Sunyaev (1973) and Frank et al. (2002), and using the results obtained in Section 3.2 for the generalised thin disc embedded within the RAR DM distribution, the set of disc equations results in:

1. $\rho = \Sigma/H$,
2. $H = c_s \left(\frac{GM(r)}{r} + G\frac{dM(r)}{dr} \right)^{-1/2} r$,
3. $c_s^2 = P/\rho$,
4. $P = \frac{\rho(r)kT_c}{\mu m_p} + \frac{4\sigma}{3c}T_c^4$,
5. $\frac{4\sigma T_c^4}{3\tau} = \frac{3\dot{M}}{8\pi} \frac{GM(r)}{r^3} \left[1 - \left(\frac{M_{in}r_{in}}{M(r)r} \right)^{1/2} \right] \left(1 - \frac{r}{3M(r)} \frac{dM(r)}{dr} \right)$,
6. $\tau = \Sigma\kappa_R(\rho, T_c) = \tau(\Sigma, \rho, T_c)$,
7. $\eta\Sigma = \frac{\dot{M}}{3\pi} \left[1 - \left(\frac{M_{in}r_{in}}{M(r)r} \right)^{1/2} \right] \frac{1}{1 - \frac{r}{3M(r)} \frac{dM(r)}{dr}}$,
8. $\eta = \eta(\rho, T_c, \Sigma, \alpha, \dots)$.

It is worth mentioning that in the limits $M(r) \to M$ and $\frac{dM(r)}{dr} \to 0$, the standard disc solutions are recovered.

There are three distinct regions in the disc, determined by the relevant absorption mechanism, and the importance of P_{rad} versus P_{gas}. Regarding the absorption mechanisms, we consider two main processes: free-free absorption, where the opacity is given by (see e.g. Shakura & Sunyaev (1973))

$$\kappa_{ff} = 5.0 \times 10^{24} \rho T_c^{-7/2} \text{ cm}^2\text{g}^{-1}, \tag{A.2}$$

and scattering, where we adopt

$$\kappa_{sc} = \frac{\sigma_T}{m_p} \sim 0.4 \text{ cm}^2\text{g}^{-1}. \tag{A.3}$$

The parameterisation of the complete solutions, together with the regions where P_{gas} dominates over P_{rad} (and vice versa), can be found in Appendix A.

As in the standard solution, there are three distinct regions in the disc: (a) an inner region, where $P_{rad} \gg P_{gas}$ and $\kappa_{es} \gg \kappa_{ff}$, (b) an intermediate region, where $P_{gas} \gg P_{rad}$ and $\kappa_{es} \gg \kappa_{ff}$, and (c) an outer region, where $P_{gas} \gg P_{rad}$ and $\kappa_{es} \ll \kappa_{ff}$. The complete solution of the set of Eqs. 1-8 for the inner, intermediate, and outer regions are presented in Eqs. A.7-A.9, A.14-A.19, and A.20-A.26, respectively. We define $R_{10} = r/(10^{10} \text{ cm})$, $m_1 = M(r)/M_\odot$, $\dot{M}_{16} = \dot{M}/(10^{16} \text{ g s}^{-1})$, $f^4 = 1 - \left(\frac{M_{in}r_{in}}{M(r)r} \right)^{1/2}$, $A = \left(\frac{M(r)}{r} + \frac{dM}{dr} \right)$, and $B = 1 - \frac{r}{3M(r)} \frac{dM(r)}{dr}$ and we consider $\mu = 0.615$ for a fully ionised gas.

It is worth noting that the limits $\frac{dm_1}{dR_{10}} \to 0$ and $M(r) \to M_{in}$ recover the standard disc solution around a compact object of a given mass M. Secondly, the α power is of the same order of magnitude as the standard solution. Hence, as α powers are low, the magnitudes calculated for the disc are not sensitive to the value of α.

The transition radii between the regions result in

$$R_{ab} \approx 3.9 \times 10^7 \alpha^{1/16} m_1^{1/2} f^2 \dot{M}_{16}^{1/2} B^{1/2} A^{-11/32} \text{ cm}, \tag{A.4}$$

$$R_{bc} \approx 2.2 \times 10^5 m_1^{1/2} f^2 \dot{M}_{16}^{1/2} B^{1/2} A^{-1/4} \text{ cm}. \tag{A.5}$$

Inner region of the disc: $P_{rad} \gg P_{gas}$ and $\kappa_{es} \gg \kappa_{ff}$:

$$\Sigma = 5.0 \times 10^8 \alpha^{-4/5} f^{12/5} B^{-2} A m_1^{1/5} \dot{M}_{16}^{3/5} R_{10}^{-3/5} \text{ g cm}^{-2}; \tag{A.6}$$

$$H = 1.4 \times 10^4 m_1^{-7/20} R_{10}^{21/20} \dot{M}_{16}^{1/5} f^{4/5} \text{cm}; \tag{A.7}$$

$$\rho = 3.7 \times 10^4 \alpha^{-4/5} f^{8/5} B^{-2} A m_1^{11/20} \dot{M}_{16}^{2/5} R_{10}^{-33/20} \text{ g cm}^{-3}; \tag{A.8}$$

$$T_c = 7.7 \times 10^5 \alpha^{-1/5} m_1^{3/10} B^{-1/2} A^{1/4} R_{10}^{-9/10} \dot{M}_{16}^{2/5} f^{8/5} K; \tag{A.9}$$

$$\tau = 2.3 \times 10^{17} \alpha^{-4/5} f^{12/5} B^{-2} A m_1^{1/5} \dot{M}_{16}^{3/5} R_{10}^{-3/5}; \tag{A.10}$$

$$\eta = 9.4 \times 10^7 \alpha m_1^{13/20} A^{-1/2} R_{10}^{-19/20} \dot{M}_{16}^{2/5} f^{24/5} \text{cm}^2 \text{ s}^{-1}; \tag{A.11}$$

$$v_R = 9.4 \times 10^{-3} m_1^{13/20} A^{-1/2} R_{10}^{39/20} \dot{M}_{16}^{2/5} f^{24/5} \text{cm s}^{-1}. \tag{A.12}$$

Intermediate region: $P_{gas} \gg P_{rad}$ and $\kappa_{es} \gg \kappa_{ff}$:

$$\Sigma = 9.9\alpha^{-4/5} f^{12/5} m^{-1/5} \dot{M}_{16}^{3/5} R_{10}^{-1/5} A^{2/5} B^{-1} \text{ g cm}^{-2}; \tag{A.13}$$

$$H = 9.6 \times 10^7 \alpha^{-1/10} m_1^{1/10} \dot{M}_{16}^{1/5} R_{10}^{3/5} f^{4/5} A^{-9/20} \text{cm}; \tag{A.14}$$

$$\rho = 1.0 \times 10^{-7} \alpha^{-7/10} m_1^{-3/10} \dot{M}_{16}^{2/5} R_{10}^{-4/5} f^{8/5} A^{13/20} B^{-1} \text{ g cm}^{-1}; \tag{A.15}$$

$$T_c = 9.2 \times 10^3 \alpha^{-1/5} M^{1/5} \dot{M}_{16}^{2/5} R_{10}^{-4/5} f^{8/5} A^{1/10} K; \tag{A.16}$$

$$\tau = 6.9 \times 10^4 \alpha^{-4/5} f^{-8/5} m_1^{-6/5} \dot{M}_{16}^{-2/5} R_{10}^{9/5} A^{7/10} B^{-2}; \tag{A.17}$$

$$\eta = 4.3 \times 10^9 \alpha^{9/10} A^{-9/20} R_{10}^{3/5} m_1^{1/10} \dot{M}_{16}^{1/5} f^{4/5} \text{cm}^2 \text{ s}^{-1}; \tag{A.18}$$

$$v_R = 4.3 \times 10^{-1} \alpha^{9/10} A^{-9/20} R_{10}^{-2/5} m_1^{1/10} \dot{M}_{16}^{1/5} f^{4/5} \text{cm s}^{-1}. \tag{A.19}$$

Outer region: $P_{gas} \gg P_{rad}$ and $\kappa_{es} \ll \kappa_{ff}$:

$$\Sigma = 3.65\alpha^{-4/5} A^{7/20} R_{10}^{-2/5} f^{14/5} B^{-9/10} \dot{M}_{16}^{7/10} m_1^{-1/10} \text{g cm}^{-2}; \tag{A.20}$$

$$H = 1.5 \times 10^8 \alpha^{-1/10} f^{3/5} \dot{M}_{16}^{3/20} R_{10}^{7/10} m_1^{1/20} A^{-17/40} B^{-1/20} \text{cm}; \tag{A.21}$$

$$\rho = 2.4 \times 10^{-8} \alpha^{-7/10} R_{10}^{-11/10} f^{11/5} \dot{M}_{16}^{11/20} m_1^{-3/20} A^{31/40} B^{-17/20} \text{g cm}^{-3}; \tag{A.22}$$

$$T_c = 2.5 \times 10^4 \alpha^{-1/5} R_{10}^{-3/5} \dot{M}_{16}^{3/10} f^{6/5} m_1^{1/10} A^{3/20} B^{-1/10} K; \tag{A.23}$$

$$\tau = 177\alpha^{-4/5} R_{10}^{3/5} f^{4/5} \dot{M}_{16}^{1/5} m_1^{-3/5} A^{3/5} B^{-7/5}; \tag{A.24}$$

$$\eta = 2.7 \times 10^{14} \alpha^{4/5} f^{6/5} \dot{M}_{16}^{3/10} R_{10}^{2/5} m_1^{1/10} A^{-7/20} B^{-1/10} \text{ cm}^2 \text{ s}^{-1}; \tag{A.25}$$

$$v_R = 2.7 \times 10^4 \alpha^{4/5} f^{-14/5} \dot{M}_{16}^{3/10} R_{10}^{-3/5} m_1^{1/10} A^{-7/20} B^{9/10} \text{cm s}^{-1}. \tag{A.26}$$

We now consider the case of models A2 and B2 described in Table 1. We assume $\dot{M} = 0.1M_{Edd} \approx 1.4 \times 10^{23}$ g s^{-1}, and $\alpha = 0.1$. We also compare to the standard disc around a Schwarzschild black hole of mass $M_{BH} = 10^7 M_\odot$.

Fig. A.1 shows the variation of both contributions to the total pressure in the different regions; in an analogous way, in Fig. A.2 we show the absorption coefficients due to scattering and free-free absorption. In both cases, we compare our models (centre and right) to the standard disc around a black hole (left).

An interesting result is obtained when varying the fermion mass from 200 keV to 48 keV (for the same mass of the core, model A2); in this case, only the outer region exists. This is due
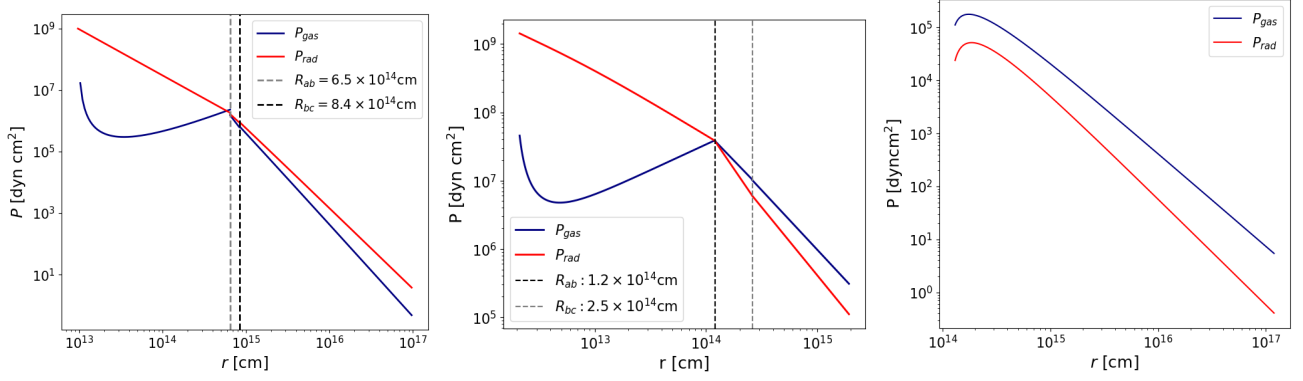
Fig. A.1. Variation of the radiation and gas pressures for a disc around a black hole (left), the RAR solution B2 (centre), and the RAR solution A2 (right). Dashed black and grey lines represent the limits of the different regions.
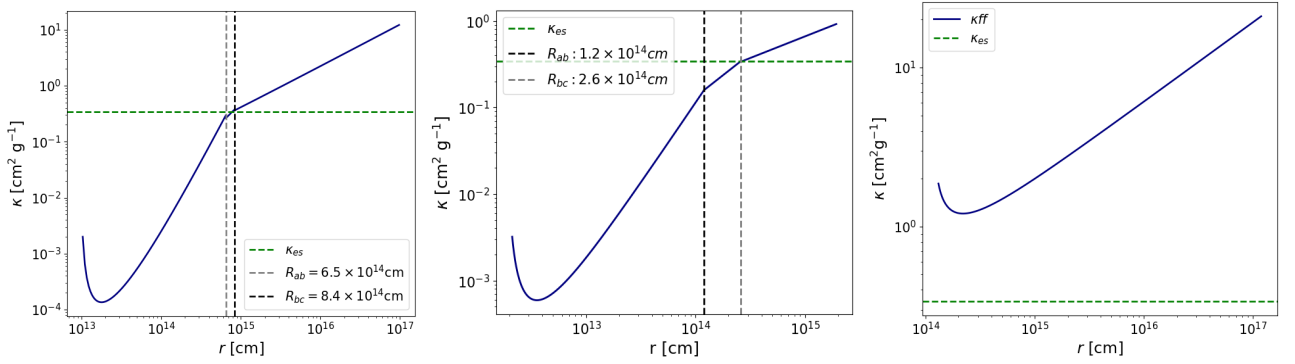
Fig. A.2. Variation of the absorption coefficients for a disc around a black hole (left), the RAR solution B2 (centre). and the RAR solution A2 (right). Dashed black and grey lines represent the limits of the different regions.
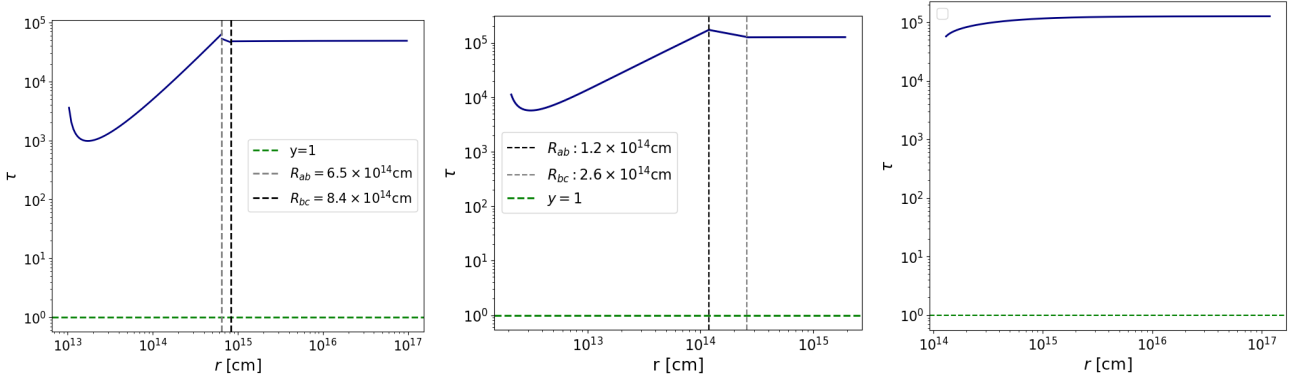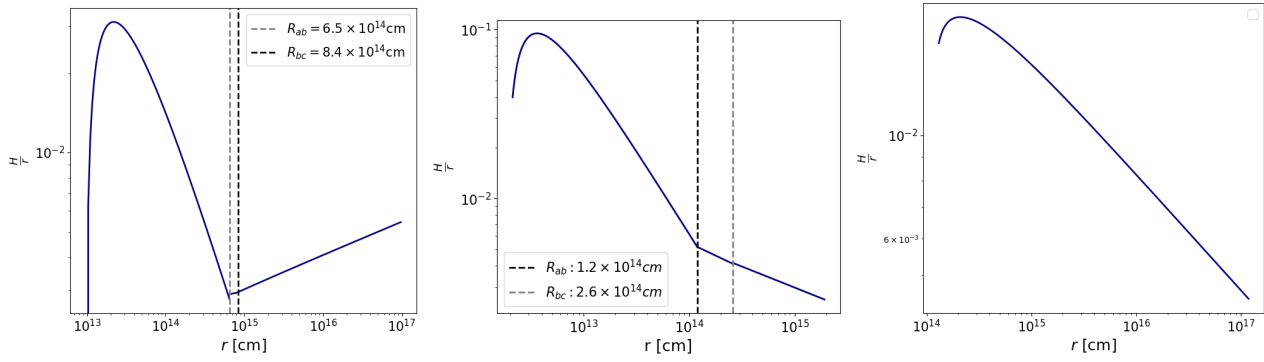

Fig. A.3. Variation of the opacity for a disc around a black hole (left), the RAR solution B2 (centre). and the RAR solution A2 (right). Dashed black and grey lines represent the limits of the different regions.

to the fact that the compacity of the core diminishes for lower masses of the fermion, which allows the disc to reach lower temperatures, as can be seen in Fig. 5.

Using the criterion given by Eq. 17, we can determined the outer radius of the disc. For both, model B2 and the black hole, $r_{\text{out}} = 1.9 \times 10^{15}$cm and $r_{\text{out}} = 1.0 \times 10^{14}$cm, respectively, which implies $r_{\text{out}} \approx 10^3 \, r_{\text{g}}$ in both cases. It is interesting to analyse model A2, where only the outer region of the disc is present. In this case, we find that the disc becomes self-gravitating at $r_{\text{out}} = 1.3 \times 10^{16}$cm $\approx 10^4 r_{\text{g}}$.

Fig. A.4. Thin disc approximation for a disc around a black hole (left), the RAR solution B2 (centre). and the RAR solution A2 (right). Dashed black and grey lines represent the limits of the different regions.